Effect of Internal Radiative Heat Transfer on Melt/Crystal Interface Shape in Czochralski Growth of Oxide Crystals

Masaki KOBAYASHI*, Takako HAGINO**, Takao TSUKADA***
and Mitsunori HOZAWA****

Abstract

A global analysis of heat transfer was carried out to investigate the effect of internal radiative heat transfer in the crystal and/or melt on the melt/crystal interface shape in Czochralski growth of an oxide crystal. As a result, it was found that the interface shapes change from convex to concave toward the melt as the crystal rotation rate increases, and that the critical Reynolds number at which the interface inversion occurs decreases with the optical thickness of the crystal when the melt is opaque. However, when the melt is semitransparent and its optical thickness is the same as the crystal's, the critical Reynolds number has a maximum value for a certain optical thickness of the crystal and melt.

Key words: Internal radiative heat transfer, Interface inversion, CZ crystal growth, Oxide, Global analysis of heat transfer

1. Introduction

Oxide single crystals such as yttrium aluminum garnet, gadolinium gallium garnet and lithium niobate are utilized as solid-state laser hosts and materials for acoust-opt-electronic devices, and are commonly grown by the Czochralski (CZ) method. For the production of a perfect oxide single crystal by the CZ method, it is important to acquire accurate information about the heat transfer mechanism and then to control the heat transfer in the CZ furnace, because the quality of the crystal is closely related to its thermal history and the transport phenomena in the furnace.

Oxide single crystals are not opaque to infrared radiation, so the radiative heat absorption and emission in the crystal strongly influence the heat transfer behavior and the shape of the melt/crystal interface during the CZ crystal growth. For instance, it is experimentally known that the radiative heat transfer through the crystal renders the interface deeply convex toward the melt [1, 2], and that the change in the absorption coefficient of the crystal affects the growth characteristics [3, 4]. Recently, such influences of the radiative heat transfer in the oxide crystal on the crystal growth behavior have also been demonstrated numerically with the

Received December 17, 2004
* Department of Chemical Engineering on Biological Environment, Lecturer
** Institute of Multidisciplinary Research for Advanced Materials, Tohoku University, Student
*** Institute of Multidisciplinary Research for Advanced Materials, Tohoku University, Associate Professor
**** Institute of Multidisciplinary Research for Advanced Materials, Tohoku University, ex-Professor

global analysis of heat transfer [5-7].

Most of the above studies have mainly focused on the effect of the radiative heat transfer in the oxide crystal. However, recent experimental studies [8-10] have suggested the possibility of the influence of the radiative heat transfer in the melt on the crystal growth processes, particularly on the melt convection. Therefore, Kobayashi *et al*. [11] numerically investigated the effect using the "bulk flow" model, and indicated that the flow and temperature fields in the melt change considerably with the variance of the absorption coefficient. They also calculated the effect of the radiative heat transfer in the melt on the transition of the flow modes with the increase of crystal rotation [12].

Since the Prandtl number of the oxide melt is relatively high, the melt convection influences the heat transfer in the melt, and consequently, the melt/crystal interface shape. In the CZ crystal growth of oxides, it is well known that the melt/crystal interface changes abruptly from convex to concave toward the melt as the crystal rotation rate or crystal diameter increases. This abrupt change, called "interface inversion", is considered to be caused by the change of the dominant melt flow near the interface from free convection to forced convection driven by crystal rotation. Therefore, the relation between the melt convection and interface inversion has been investigated numerically in many previous works [5, 6, 13-16], because the interface shape during the crystal growth is closely related to the crystal quality. In most of these works, the crystal was considered to be opaque, except in that of Xiao and Derby [5, 6] who numerically demonstrated the effect of the radiative heat transfer in the crystal on the interface inversion assuming the crystal to be totally transparent. However, the oxide crystals are often semitransparent and their absorption coefficients vary depending on the amount of dopant added, such as in Cockayne's experimental work [1]. Thus, a more rigorous model for a radiative heat transfer, i.e., a model taking into account semitransparency of crystal and/or melt, is necessary to numerically investigate the interface shape in the CZ growth of an oxide crystal.

The aim of the present work is to numerically investigate the effect of variations in the absorption coefficients of the crystal and/or melt on the interface shape, using the global model in which the radiative heat transfer in the crystal and/or melt can be accounted for.

2. Theory

In the CZ growth of an oxide crystal, radio-frequency (RF) induction heating, as shown in Fig. 1, is commonly used. The ac electric current in the coil induces the eddy current in the metal crucible wall, and consequently, the raw material of the crystal inside the crucible is melted by the Joule heating from the eddy current. Therefore, in the global analysis of heat transfer in the inductively heated CZ furnace, the electromagnetic field in the system should be computed first to obtain the distributions of the eddy current, i.e., heat power in the crucible and the after heater ; then flow and temperature fields in the furnace as well as the shapes of the melt/gas interfaces are calculated.

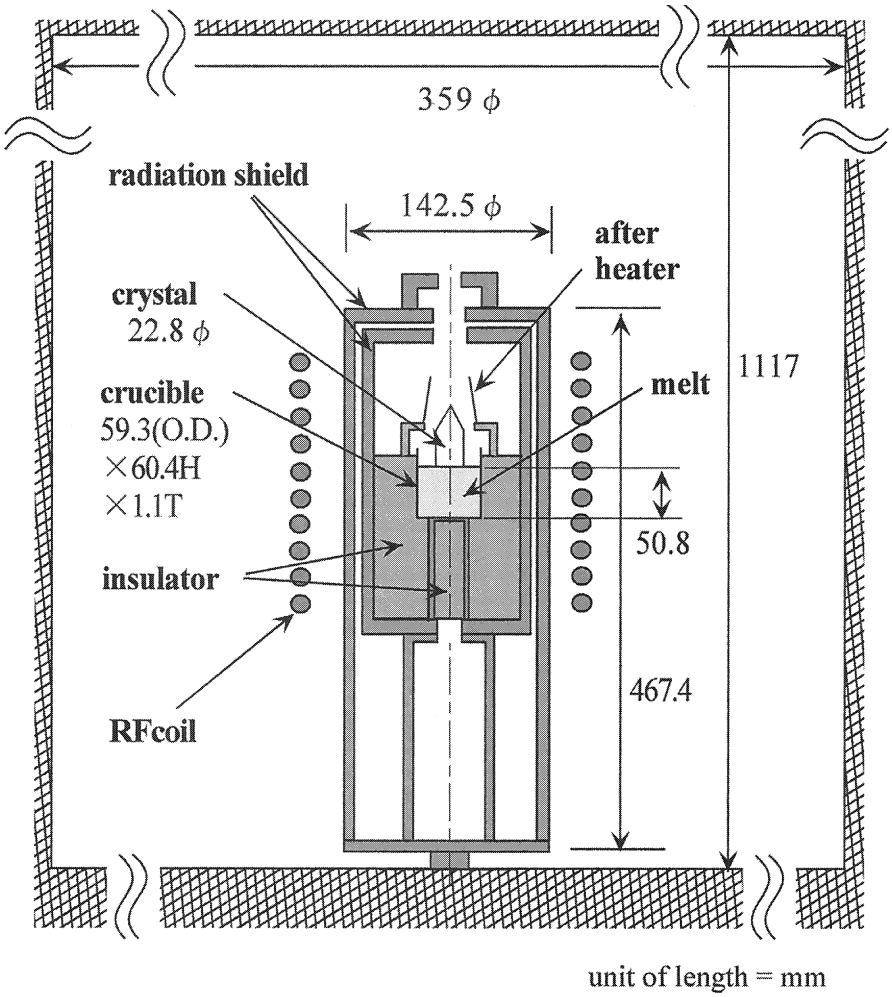

Fig. 1 Schematic diagram of the inductively heated CZ furnace.

In the previous works, we developed a mathematical model with which we can predict the electromagnetic, flow and temperature fields in the furnace and the interface shapes [16], and subsequently extended the model by incorporating the P_1 method to account for the internal radiation within the crystal and the melt [7]. For brevity, mathematical details of calculating the electromagnetic field in the furnace are not included here, but are available in our previous work [16]. However, the rest of the model is described below because some modifications have been made.

The dimensionless forms of the governing equations of melt convection, i.e., the continuity equation and the momentum equation based on the Boussinesq approximation, are expressed as follows, assuming that the system is axisymmetric and in the quasi-steady state and that the melt is laminar and Newtonian.

$$\nabla \cdot \boldsymbol{\nu}_l = 0. \tag{1}$$

$$\boldsymbol{\nu}_l \cdot \nabla \boldsymbol{\nu}_l = -\nabla p_l - \nabla \cdot \boldsymbol{\tau}_l + Gr(T_l - 1)\boldsymbol{e}_z. \tag{2}$$

Here, Gr is the Grashof number defined by $\beta' g' T'_m r'^3_c / \nu'^2_l$. The length is scaled with the crucible radius r'_c, velocity with ν'_l / r'_c, the pressure and stress with $\rho'_{0,l}$, ν'^2_l / r'^2_c, and the temperature with the melting temperature T'_m, in which the superscript " ' " refers to the dimensional value.

The dimensionless energy equations are given as follows.

Melt : $$Pr\boldsymbol{\nu}_l \cdot \nabla T_l = \nabla^2 T_l + \boldsymbol{\kappa}_l N_R (J_l - n_l^2 T_l^4). \tag{3}$$

Crystal : $$Pe\boldsymbol{e}_z \cdot \nabla T_s = \boldsymbol{\kappa}_s \nabla^2 T_s + \boldsymbol{\kappa}_s N_R (J_s - n_s^2 T_s^4). \tag{4}$$

Crucible and after heater : $$K_i \nabla^2 T_i + \alpha Q_0 = 0 \qquad (i = c, h). \tag{5}$$

Elsewhere : $$K_i \nabla^2 T_i = 0. \tag{6}$$

Pr, Pe and K_i are the Prandtl number, Peclet number and thermal conductivity ratios to that of the melt, defined by $\mu'_l C'_{pl} / k'_l$, $\rho'_{0,s} C'_{p,s} V'_s r'_c / k'_l$ and k'_i / k'_l, respectively. Q_0 is the dimensionless heat generation rate by the Joule heat in the crucible and after heater for a reference value of the electric current in the RF coil, and is obtained from the analysis of the electromagnetic field in the furnace. In the heat transfer analysis, α is determined as a part of the solutions so that the temperature at the tri-junction may be the melting point, on the basis of the fact that the local heat generation rate is proportional to the square of the current density in the coil. The subscripts "l, s, c and h" in the above equations indicate the melt, crystal, crucible and after heater, respectively.

In Eqs.(3) and (4), the second terms on the right-hand side represent the contribution of the radiative heat transfer, in which $\boldsymbol{\kappa}$ and N_R are the optical thickness and radiation-conduction interaction parameter defined by $\alpha' r'_c$ and $4\sigma' T'^3_m r'_c / k'_l$, respectively. In the present work, the optical absorption coefficient α' is independent of the wavelength, since we consider the radiative heat transfer in gray absorbing-emitting media. n_l and n_s are the refractive indices of the melt and crystal. J is the irradiance defined by the zeroth-order moment of radiative intensity i, i.e.,

$$J = \int_{\omega = 4\pi} i d\omega, \tag{7}$$

and is governed by the following equations which represent an approximation of the equation of transfer in a nonscattering medium with the P_1 model [17].

Melt : $$\frac{1}{3\boldsymbol{\kappa}_l} \nabla^2 J_l = \boldsymbol{\kappa}_l (J_l - n_l^2 T_l^4). \tag{8}$$

Crystal : $$\frac{1}{3\boldsymbol{\kappa}_s} \nabla^2 J_s = \boldsymbol{\kappa}_s (J_s - n_s^2 T_s^4). \tag{9}$$

J is scaled with $4\sigma' T'^4_m$.

The boundary conditions for Eqs.(1)-(6), (8) and (9) are given by the following equations.

At the melt/crystal interface :

$$\boldsymbol{\nu}_l \cdot \boldsymbol{n}_{ls} = \boldsymbol{\nu}_l \cdot \boldsymbol{t} = 0,\ \boldsymbol{\nu}_l \cdot \boldsymbol{e}_\theta = rRe,\ T_l = T_s = 1, \tag{10a-e}$$

$$-\nabla T_l \cdot \boldsymbol{n}_{ls} + K_s \nabla T_s \cdot \boldsymbol{n}_{ls} = -PeSt(\boldsymbol{e}_z \cdot \boldsymbol{n}_{ls}), \tag{10f}$$

$$\frac{1}{3\boldsymbol{\kappa}_l} \nabla J_l \cdot \boldsymbol{n}_{ls} = \frac{1}{3\boldsymbol{\kappa}_s} \nabla J_s \cdot \boldsymbol{n}_{ls}. \tag{10g}$$

At the melt/gas interface:

$$\boldsymbol{\nu}_l \cdot \boldsymbol{n}_{lg} = 0,\ \boldsymbol{\tau}_l :\ \boldsymbol{n}_{lg}\boldsymbol{t} = \boldsymbol{\tau}_l :\ \boldsymbol{n}_{lg}\boldsymbol{e}_\theta = \boldsymbol{0}, \tag{11a-c}$$

$$\nabla T_l \cdot \boldsymbol{n}_{lg} = 0, \tag{11d}$$

$$-\frac{1}{3\boldsymbol{\kappa}_l} \nabla J_l \cdot \boldsymbol{n}_{lg} = \frac{1}{2}\left(\frac{1-\rho_l^{in}}{1+\rho_l^{in}}\right)(J_l - n_l^2 q_{i,l}^{out}). \tag{11e}$$

At the crucible wall:

$$\boldsymbol{\nu}_l \cdot \boldsymbol{n}_{ls} = \boldsymbol{\nu}_l \cdot \boldsymbol{t} = \boldsymbol{\nu}_l \cdot \boldsymbol{e}_\theta = 0, \tag{12a-c}$$

$$-\nabla T_l \cdot \boldsymbol{n}_{lc} + K_c \nabla T_c \cdot \boldsymbol{n}_{lc} = -\frac{\varepsilon_c N_R}{2(2-\varepsilon_c)}(J_l - n_l^2 T_l^4), \tag{12d}$$

$$-\frac{1}{3\boldsymbol{\kappa}_l} \nabla J_l \cdot \boldsymbol{n}_{lc} = \frac{\varepsilon_c}{2(2-\varepsilon_c)}(J_l - n_l^2 T_l^4). \tag{12e}$$

At the crystal surface:

$$\nabla T_s \cdot \boldsymbol{n}_{sg} = 0, \tag{13a}$$

$$-\frac{1}{3\boldsymbol{\kappa}_s} \nabla J_s \cdot \boldsymbol{n}_{sg} = \frac{1}{2}\left(\frac{1-\rho_s^{in}}{1+\rho_s^{in}}\right)(J_s - n_s^2 q_{i,s}^{out}). \tag{13b}$$

Elsewhere:

$$-K_j \nabla T_j \cdot \boldsymbol{n}_{jg} = \frac{\varepsilon_j N_R}{4}(T_j^4 - q_{i,j}^{out}). \tag{14a}$$

At the centerline:

$$\boldsymbol{\nu}_1 \cdot \boldsymbol{n}_{cl} = \boldsymbol{\nu}_l \cdot \boldsymbol{e}_\theta = 0,\ \boldsymbol{\tau}_l :\ \boldsymbol{n}_{cl}\boldsymbol{t} = 0, \tag{15a-c}$$

$$\nabla T_l \cdot \boldsymbol{n}_{cl} = \nabla T_s \cdot \boldsymbol{n}_{cs} = \nabla T_c \cdot \boldsymbol{n}_{cl} = \nabla T_j \cdot \boldsymbol{n}_{cj} = 0, \tag{15d-g}$$

$$\nabla J_l \cdot \boldsymbol{n}_{cl} = \nabla J_s \cdot \boldsymbol{n}_{cs} = 0, \tag{15h, i}$$

where Re and St are the Reynolds number based on the crystal rotation rate and the Stefan number, defined by $r_c'^2\Omega'/\nu_l'$ and $\Delta H_f'/C_{ps}'T_m'$, respectively. The Marangoni convection in the melt is not considered here, as shown in Eqs.(11b, c). In the CZ crystal growth system, each material constituting the furnace, such as the melt, the crystal and the crucible, is surrounded by a transparent gas, and the incident radiative heat flux to their surfaces through the ambient gas, i.e., irradiation q_i^{out}, is partially absorbed and reflected if the material is opaque. In the case of the semitransparent material, moreover, a part of the irradiation transmits inside the material. Thus, the boundary conditions for temperature and irradiance, Eqs.(11e), (13b) and (14a), include q_i^{out}. The superscripts "*out*" and "*in*" refer to the outside and inside of the surface adjoining the surrounding gas, respectively, and the subscript "*i*" of q_i^{out} implies the incident flux.

To solve the above governing equations with the boundary conditions, q_i^{out} should be given

explicitly. Here, let us consider that the gas phase in the CZ furnace shown in Fig. 1 is the enclosure surrounded by N opaque and semitransparent diffuse-gray surfaces of uniform temperature. The irradiation onto a surface j, $q_{i,j}^{out}$ is given by the following equation, creating an energy balance regarding the surface j in the enclosure:

$$q_{i,j}^{out}=\frac{1}{1-\rho_j^{out}}(\varepsilon_j T_j^4+\tau_j^{in}q_{i,j}^{in}-q_j), \tag{16}$$

where $q_{i,j}^{in}$ is the incident radiative heat flux on the inside of a semitransparent surface j such as the crystal surface, and is expressed with the irradiance J as

$$q_{i,j}^{in}=J_j-\frac{2}{3\boldsymbol{\kappa}_j}\nabla J_j\cdot\boldsymbol{n}_{sg}. \tag{17}$$

In addition, the net radiative heat flux at surface j, q_j in Eq.(16), is obtained as a solution of the following matrix equations which govern radiative heat transfer in the enclosure:

$$\left(\frac{1}{1-\rho_j}\right)q_j-\sum_{k=1}^{N}\frac{\rho_k}{1-\rho_k}F_{jk}q_k=\frac{1}{1-\rho_j}(\varepsilon_j T_j^4+\tau_j^{in}q_{i,j}^{in})-\sum_{k=1}^{N}\frac{1}{1-\rho_k}F_{jk}(\varepsilon_k T_k^4+\tau_k^{in}q_{i,k}^{in})\quad(j=1, 2, \ldots\ldots, N), \tag{18}$$

where F_{jk} is the view factor which is calculated efficiently by combining the analytical solutions [16]. If the material with surface j is opaque, the transmissivity τ_j in Eqs.(16) and (18) is set to be zero, while the emissivity ε_j is neglected in the case of semitransparent materials.

Eqs.(3), (8) and (10)-(12) are the governing equations and the boundary conditions for the semitransparent melt. While, in the case of the opaque melt, the second (radiative) term on the right-hand side in Eq.(3) are eliminated, in addition to complete elimination of Eqs.(8), (11e) and (12e). Moreover, the boundary conditions, Eqs.(10f), (10g), (11d) and (12d), are replaced by the following equations, Eqs.(19a), (19b), (20) and (21), respectively.

At the melt/crystal interface:

$$-\nabla T_l\cdot\boldsymbol{n}_{ls}+K_s\nabla T_s\cdot\boldsymbol{n}_{ls}=-\frac{\varepsilon_l N_R}{2(2-\varepsilon_l)}(J_s-n_s^2T_s^4)-PeSt(\boldsymbol{e}_z\cdot\boldsymbol{n}_{ls}), \tag{19a}$$

$$-\frac{1}{3\boldsymbol{\kappa}_s}\nabla J_s\cdot\boldsymbol{n}_{ls}=-\frac{\varepsilon_l}{2(2-\varepsilon_l)}(J_s-n_s^2T_s^4). \tag{19b}$$

At the melt/gas interface:

$$-\nabla T_l\cdot\boldsymbol{n}_{lg}=\frac{\varepsilon_l N_R}{4}(T_l^4-q_{i,l}^{out}). \tag{20}$$

At the crucible wall:

$$\nabla T_l\cdot\boldsymbol{n}_{lc}=K_c\nabla T_c\cdot\boldsymbol{n}_{lc}. \tag{21}$$

The melt/crystal interface shape is determined so that Eq.(10e) may be satisfied, i.e., so that the interface coincides with the melting point isotherm. The melt/gas interface shape is calculated by solving the Young-Laplace equation.

The finite element method is used for the calculations of the temperature field in the furnace and velocity field in the melt, as well as the shapes of the melt/crystal and melt/gas interfaces, where the SUPG (streamline upwind Petrov-Galerkin) method [18] is applied for the treatment of the convective term. The calculation domain is discretized by 7600 isoparametric quadrilateral elements, and in each element, velocity vectors, temperature and irradiance are approximated with bilinear polynomials and the pressure is considered to be constant. After the electromagnetic field in the CZ furnace and Q_0 in Eq.(5) are calculated for a reference value of current in the RF coil and the shape of the melt/gas interface is obtained, the global analysis is carried out with the following procedure. 1) Eq.(18) is solved for the net radiative heat fluxes at the surfaces adjoining the ambient gas phase, $q_j (j=1, 2, ..., N)$, with T_j and $q_{i,j}^{in}$ obtained in the previous step. 2) The temperature and velocity fields in the furnace, the interface shape and α are calculated by simultaneously solving Eqs.(1)-(15) and (19)-(21), where q_i^{out} in the boundary conditions is calculated from Eq.(16) with T_j and $q_{i,j}^{in}$ in the previous step and q obtained in step 1. 3) Steps 1 and 2 are repeated until all equations and boundary conditions are satisfied.

3. Results and discussion

In the present work, we consider the heat transfer of an inductively heated CZ furnace with 4.6 kHz radio-frequency current, as shown in Fig. 1, where a $LiNbO_3$ single crystal (22.8 mm diameter) is pulled continuously at the rate of 4 mmh^{-1} from the melt in a Pt crucible (59.3 $mm^{O.D.} \times 60.4\ mm^{H} \times 1.1\ mm^{T}$). The physical properties of $LiNbO_3$ melt and crystal, etc. used in the calculations are identical to those used in our previous work [16]. For the optical properties, the transmissivities on both sides of the semitransparent melt and crystal surfaces are estimated with their refractive indices ($n_l = n_s = 2.3$) as [19, 20]

$$\tau_i^{out} = 1 - \rho_i^{out} = \frac{1}{2} - \frac{(3n_i+1)(n_i-1)}{6(n_i+1)^2} - \frac{n_i^2(n_i^2-1)^2}{(n_i^2+1)^3}\ln\left(\frac{n_i-1}{n_i+1}\right) + \frac{2n_i^3(n_i^2+2n_i-1)}{(n_i^2+1)(n_i^4-1)} - \frac{8n_i^4(n_i^4+1)}{(n_i^2+1)(n_1^4-1)^2}\ln(n_i) \cong 0.80, \tag{22a}$$

$$\tau_i^{in} = 1 - \rho_i^{in} = \frac{\tau_i^{out}}{n_i^2} \cong 0.15. \tag{22b}$$

On the other hand, when the melt is opaque, the emissivity of the melt into the gas phase can be estimated to be 0.80 using Eq.(22a) for $\varepsilon_l (=1-\rho_l^{out})$, and also the emissivity into the crystal is 1.0 if n_l is assumed to be equal to n_s. The absorption coefficients of the melt and crystal are varied within the limits of the optical thickness $\kappa (=a' r_c') \geq 1$ because the P_1 approximation used here is not very well adapted for optically thin materials. The Prandtl number Pr and the Grashof number Gr in this system are 13.6 and 4.67×10^5, respectively.

Fig. 2 shows the effect of the crystal rotational Reynolds number Re on the temperature distributions in the furnace and the flow pattern in the melt for two values of optical thickness of the crystal κ_s, where the melt is opaque, i.e., $\kappa_l = \infty$, and the emissivities of the melt into gas phase and the crystal are 0.8 and 1.0, respectively. The stream functions in the figures are

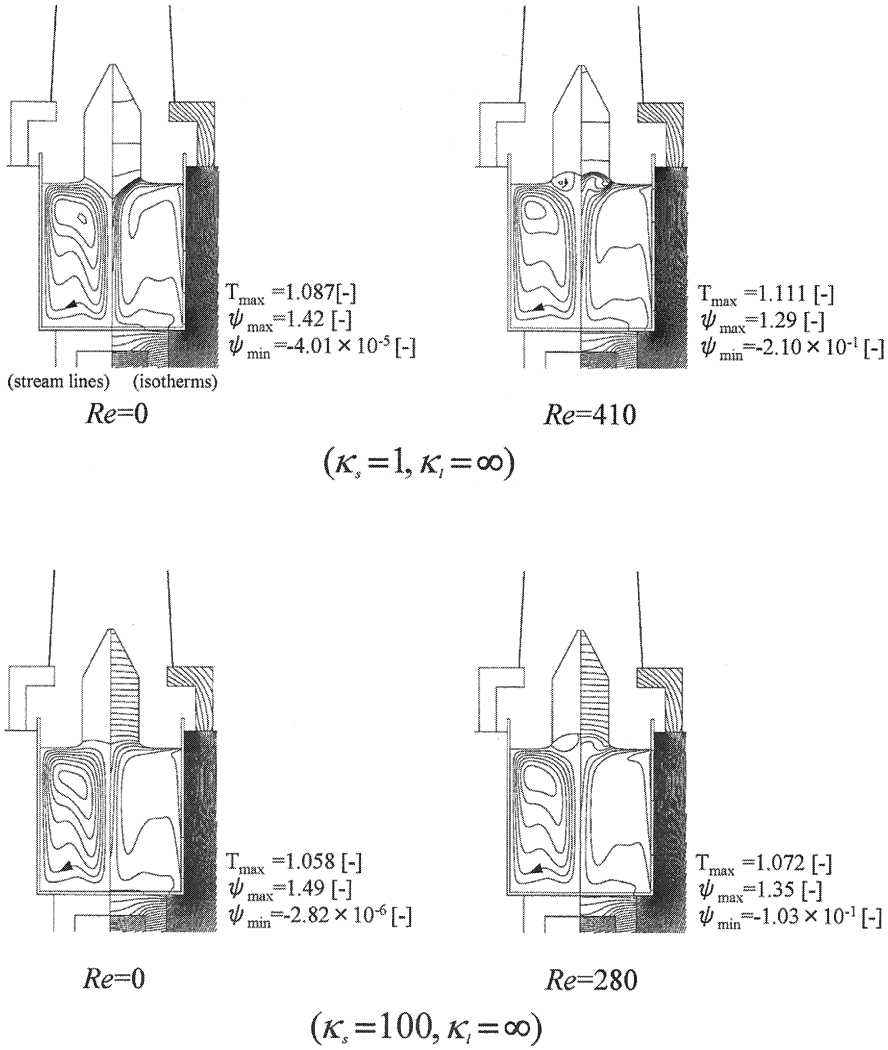

Fig. 2 Temperature distributions in the furnace and the flow pattern in the melt for $\varkappa_l=\infty$, where $\Delta T=0.01$ [—] and $\Delta \Psi=0.2$ [—].

scaled with $r'_c\nu'_l$. When the crystal is not rotated, i.e., $Re=0$, only the clockwise vortex caused by free convection is present in the melt, and the flow pattern exhibits an undulating structure at the bottom of the crucible due to a retarding force caused by the vertical stratification of the melt. On the other hand, when Re increases, a counterclockwise vortex due to crystal rotation appears under the crystal for both optical thickness $\varkappa_s=1$ and 100. Such a melt convection affects the temperature distributions in the melt and crystal because the Prandtl number of the oxide melt is relatively large (>1), but the influence of the radiative heat transfer within semitransparent crystals such as oxides is still more significant. The figures show that the temperature gradients in the crystal decrease when the optical thickness decreases, because the

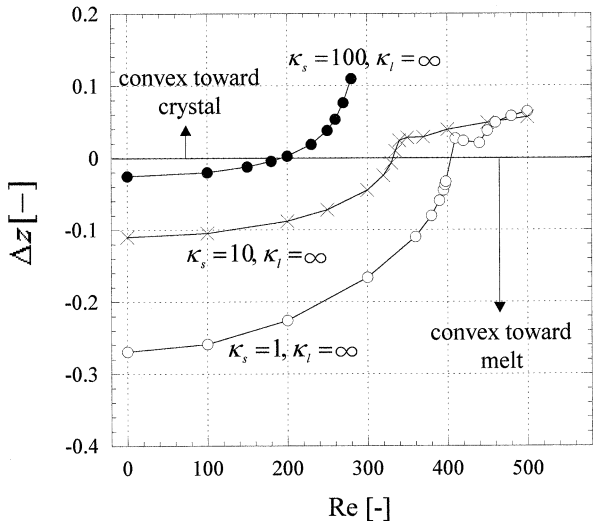

Fig. 3 Effect of the crystal rotational Reynolds number Re on the melt/crystal interface shapes for different values of optical thickness of the crystal $\varkappa_s$ and $\varkappa_l=\infty$.

contribution of the radiation to the total heat transfer through the crystal increases and the role of the thermal conduction diminishes. The larger heat flux due to the radiation through the crystal brings about the larger heat flux to the melt/crystal interface from the melt to compensate it. Consequently, it can be seen from the case of $Re=0$ in Fig. 2 that the melt/crystal interface increases its area and becomes more convex toward the melt.

Figs. 3 shows the effect of the crystal rotational Reynolds number Re on the melt/crystal interface shapes for three different values of optical thickness of the crystal and $\varkappa_l=\infty$. In these figures, Δz in represents the axial displacement of the interface at the centerline from the axial position of the melt/crystal/gas tri-junction ($r=r_s$). If Δz is negative, the interface shape can be regarded as nearly convex toward the melt. Here, we use the expression "nearly convex" because the interfaces take on a doubly curved, or 'gull-wing' geometry which is seen for $Re=410$ and $\varkappa_s=1$ in Fig. 2, in the changes of their shapes with Re. For all $\varkappa_s$, Δz increases with Re, and the melt/crystal interface shape changes from convex to a 'gull-wing' geometry, and then becomes completely concave toward the melt. Fig. 3 demonstrates numerically that the interface inversion occurs with the increase of Re. When Re is relatively small and the interface is convex toward the melt, the magnitude of the interface deflection Δz becomes larger as the optical thickness of the crystal $\varkappa_s$ decreases, and consequently Re_c shifts to a larger value, where Re_c is the critical Reynolds number defined as Re at which Δz becomes a positive value, i.e., the interface inversion occurs. In addition, the dependence of Δz on Re near Re_c becomes more remarkable as $\varkappa_s$ decreases, and thus the interface changes more abruptly. This steep increases of Δz are due to the melt flow toward the melt/crystal interface caused by the crystal rotation.

Since the recent experimental studies [8-10] revealed the possibility of the influence of the

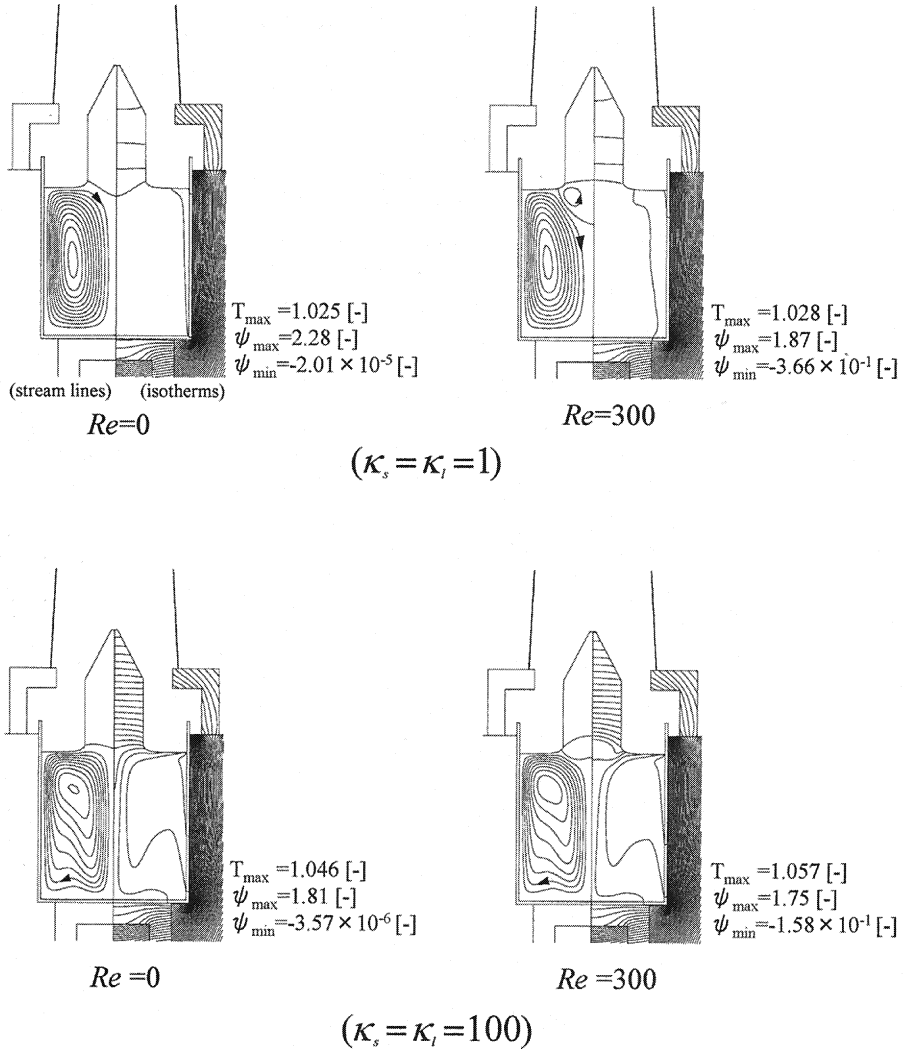

Fig. 4 Temperature distributions in the furnace and the flow pattern in the melt for $\varkappa_l=\varkappa_s$, where $\Delta T=0.01$ [—] and $\Delta \Psi=0.2$ [—].

radiative heat transfer in the melt on the crystal growth processes, particularly on the melt convection, the effect of the crystal rotation on the CZ crystal growth process should be investigated when both melt and crystal are semitransparent. Fig. 4 shows the effect of the crystal rotational Reynolds number Re on the temperature distributions in the furnace and the flow pattern in the melt for two values of optical thickness, where $\varkappa_l=\varkappa_s$ and the reflectivity of the melt, ρ_l, is 0.20 from Eq.(22a). In the case of optically thicker melt and crystal, i.e., $\varkappa_l=\varkappa_s=100$, the shapes of the temperature distributions and flow patterns are almost the same as those in Fig. 2, and the interface inversion occurs as Re increases. However, for $\varkappa_l=\varkappa_s=1$ and $Re=0$, compared with the results for $\varkappa_l=\varkappa_s=100$, the undulating flow structure near the

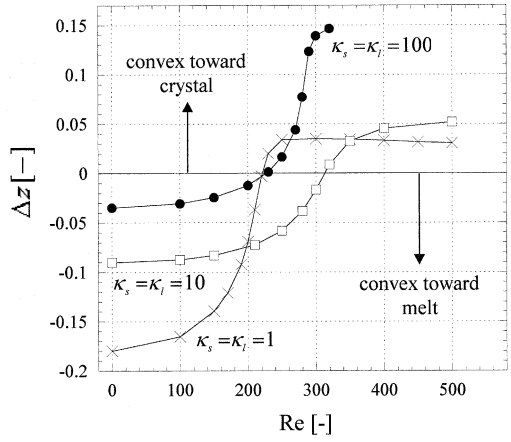

Fig. 5 Effect of the crystal rotational Reynolds number Re on the melt/crystal interface shapes for different values of optical thickness of the crystal $\varkappa_s$ and $\varkappa_l=\varkappa_s$.

crucible bottom does not appear, and a relatively simple convection with the vortex center at the middle part of the melt occurs [7]. In addition, the intensity of the convection in the melt is larger despite the decrease of the maximum temperature in the melt. These phenomena are explained as follows: the radiative energy emitted at the crucible wall is absorbed inside the melt and heats it. Also, the contribution of radiation to the total heat loss through the melt becomes larger, in other words, the conduction becomes smaller. Consequently, vertical stratification is not formed in the melt, but the horizontal temperature gradient is established in the melt and the buoyant flow becomes stronger than that in the optically thicker melt. In this case, also, the melt/crystal interface shape becomes more convex toward the melt as the optical thickness of both melt and crystal decreases.

Fig. 5 shows the effect of the crystal rotational Reynolds number Re on the melt/crystal interface shapes for three different values of optical thickness, when both melt and crystal are semitransparent and $\varkappa_l=\varkappa_s$. For all $\varkappa_s$, Δz increases in the range of relatively small Re and the melt/crystal interface changes from convex to concave toward the melt at Re_c. This is the same aspect as that in the case of the opaque melt shown in Fig. 3 although the gull-wing geometry of the interface is not observed clearly. However, Re_c for $\varkappa_s=1$ is much smaller than those for $\varkappa_s=10$. With respect to this, the temperature distributions in the furnace and the flow pattern in the melt for $\varkappa_s=1, 10$ and $Re=200$ are shown in Fig. 6. The intensity of clockwise buoyant flow for $\varkappa_s=1$ is weaker than that for $\varkappa_s=10$. Therefore, this leads to the decrease of the Re_c at which the dominant melt flow near the interface changes from free convection to forced convection driven by crystal rotation.

To sum up the behavior on the shape of the melt/crystal interface, the effect of the optical thickness of the crystal and/or melt on the Re_c for the opaque and semitransparent melt is shown in Fig. 7. It is clearly found that the Re_c, when the melt is opaque, decreases monotonically with the optical thickness of the crystal, whereas the Re_c has a maximum value

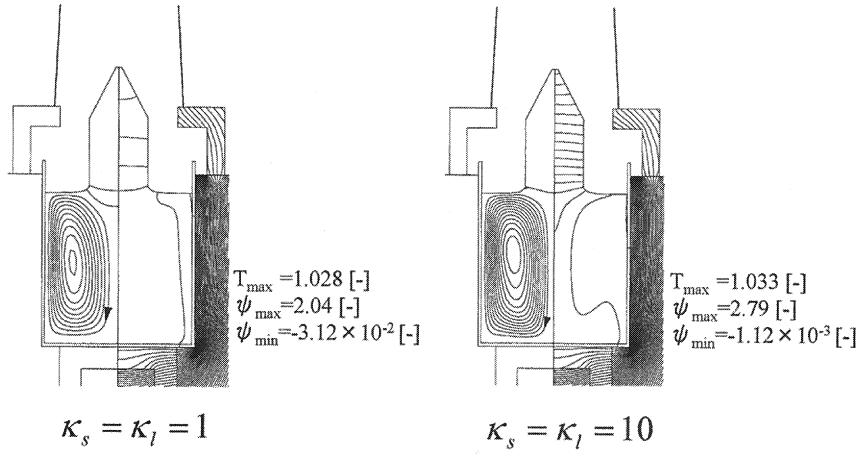

Fig. 6 Temperature distributions in the furnace and the flow pattern in the melt for $\varkappa_s$=1 and 10, where Re=200, ΔT=0.01 [—] and $\Delta \Psi$=0.2 [—].

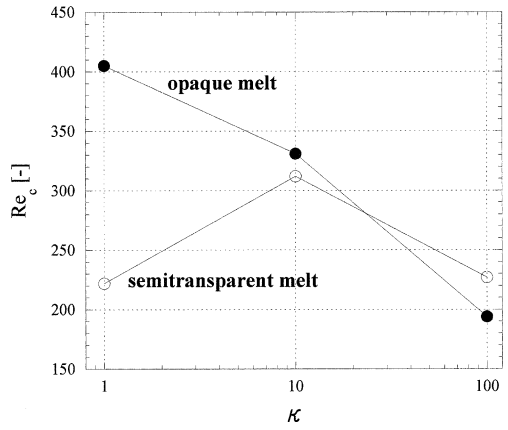

Fig. 7 Effect of the optical thickness of the crystal and/or melt on the critical Reynolds number Re_c for the opaque and semitransparent melt.

for a certain optical thickness of the crystal and melt when the melt is semitransparent and $\varkappa_l = \varkappa_s$. However, there might be oxide systems showing that the absorption coefficients of the melt and crystal are different and the conclusion regarding a maximum in Re_c for the semitransparent melt might change if the ratio of $\varkappa_l/\varkappa_s$ is changed.

4. Conclusions

For the crystal growth of an oxide, the global analysis of heat transfer in the inductively heated CZ furnace was carried out to investigate the effect of optical properties of crystal and melt on the melt/crystal interface shape, in which the radiative heat transfer in the crystal and/

or melt can be accounted for. As a result, it was found that the interface shapes change from convex to concave toward the melt as the crystal rotation rate increases, and that critical Reynolds number at which the interface inversion occurs decreases with the optical thickness of the crystal when the melt is opaque. However, when the melt is semitransparent and its optical thickness is the same as the crystal's, the critical Reynolds number has a maximum value for a certain optical thickness of crystal and melt, depending on the melt flow structure composed of the free convection and the forced convection caused by the crystal rotation.

Nomenclature

a'	=	absorption coefficient	$[m^{-1}]$
C'_p	=	heat capacity	$[J \cdot kg^{-1} \cdot K^{-1}]$
$\boldsymbol{e}$	=	unit vector	[—]
F_{jk}	=	view factor	[—]
g'	=	gravitational acceleration	$[m \cdot s^{-2}]$
Gr	=	Grashof number	[—]
$\Delta H'_f$	=	latent heat of solidification	$[J \cdot kg^{-1}]$
i	=	radiative intensity	[—]
J	=	irradiance	[—]
K	=	ratio of thermal conductivity	[—]
k'	=	thermal conductivity	$[W \cdot m^{-1} \cdot K^{-1}]$
N_R	=	radiation-conduction interaction parameter	[—]
n	=	refractive index	[—]
$\boldsymbol{n}$	=	normal unit vector	[—]
Pe	=	Peclet number	[—]
Pr	=	Prandtl number	[—]
P	=	pressure	[—]
Q_0	=	standard volumetric heat generation rate	[—]
q_j	=	net heat flux due to the incident radiation on jth boundary surface	[—]
$q_{i,j}$	=	incident radiative flux on jth boundary surface	[—]
r	=	radial position in cylindrical coordinates	[—]
r'_c	=	crucible radius	[m]
r_s	=	crystal radius	[—]
Re	=	Reynolds number	[—]
Re_c	=	critical Reynolds number	[—]
St	=	Stefan number	[—]
T	=	temperature	[—]
T'_m	=	melting temperature	[K]
$\boldsymbol{t}$	=	tangential unit vector	[—]
V'_s	=	crystal pulling rate	$[m \cdot s^{-1}]$

$\boldsymbol{\nu}$	=	velocity vector	[—]
Δz	=	axial displacement of the interface	[—]

Greek symbols

α	=	heat generation coefficient	[—]
β'	=	thermal expansion coefficient	[K^{-1}]
ε	=	emissivity	[—]
$\varkappa$	=	optical thickness	[—]
μ'	=	viscosity	[Pa•s]
ν'	=	kinematic viscosity	[m^2•s^{-1}]
ρ_0'	=	density	[kg•m^{-3}]
ρ^{in}, ρ^{out}	=	reflectivity	[—]
σ'	=	Stefan-Boltzman constant	[W•m^{-2}•K^4]
τ	=	stress tensor	[—]
τ^{in}, τ^{out}	=	transmissivity	[—]
Ψ	=	stream function	[—]
Ω'	=	crystal rotation rate	[rad•s^{-1}]
w	=	solid angle	[sr]

Superscripts

in	=	inside of boundary surface
out	=	outside of boundary surface
,	=	dimensional value

Subscripts

c	=	crucible
cj	=	pointing from centerline to material *j*
cl	=	pointing from centerline to melt
cs	=	pointing from centerline to crystal
h	=	after heater
j	=	material *j*
jg	=	pointing from material *j* to gas phase
l	=	melt
lc	=	pointing from melt to crucible
lg	=	pointing from melt to gas phase
ls	=	pointing from melt to crystal
max	=	maximum value
min	=	minimum value
s	=	crystal
sg	=	pointing from crystal to gas phase

z = z-direction
θ = θ-direction

References

[1] B. Cockayne, M. Chesswas and D.B. Gasson, *J. Mater. Sci.* **4**(1969) 450.
[2] Ji. Kvapil, Jo. Kvapil, B. Manek, B. Perner, R. Autrata and P. Scuer, *J. Crystal Growth* **52**(1981) 542.
[3] C.D. Brandle, V.J. Fratello, A.J. Valentine and S.E. Stokowski, *J. Crystal Growth* **85**(1987) 223.
[4] Y. Okano, Y. Tsuji, D.H. Yoon, K. Hoshikawa and T. Fukuda, *J. Crystal Growth* **141**(1994) 383.
[5] Q. Xiao and J.J. Derby, *J. Crystal Growth* **128**(1994) 188.
[6] Q. Xiao and J.J. Derby, *J. Crystal Growth* **139**(1994) 147.
[7] T. Tsukada, K. Kakinoki, M. Hozawa and N. Imaishi, *Int. J. Heat Mass Transfer* **38**(1995) 2707.
[8] Y. Okano, Y. Tsuji, D.H. Yoon and T. Fukuda, *J. Mat. Process. Manufact. Sci.* **4**(1995) 1.
[9] Y. Miyazawa, S. Morita and H. Sekiwa, *J. Jpn. Crystal Growth* **19**(1992) 14.
[10] S. Morita, H. Sekiwa and Y. Miyazawa, *J. Jpn. Crystal Growth* **19**(1992) 69.
[11] M. Kobayashi, T. Tsukada and M. Hozawa, *J. Crystal Growth* **180**(1997) 157.
[12] M. Kobayashi, T. Tsukada and M. Hozawa, *J. Crystal Growth* **208**(2000) 459.
[13] T. Tsukada, N. Imaishi and M. Hozawa, *J. Chem. Eng Japan* **21**(1988) 184.
[14] H. Kopetsch, *J. Crystal Growth* **102**(1990) 575.
[15] J.J. Derby and Q. Xiao, *J. Crystal Growth* **113**(1991) 575.
[16] T. Tsukada, M. Hozawa and N. Imaishi, *J. Chem. Eng. Japan* **27**(1994) 25.
[17] M.F. Modest, *Radiative Heat Transfer*, McGraw-Hill, New York, 1993.
[18] A.N. Brooks and T.J.R. Hughes, *Comp. Meth. Appl. Mech. Engrg.* **32**(1982) 199.
[19] C.M. Spuckler and R. Siegel, *J. Thermopysics Heat Transfer* **4**(1992) 596.
[20] C.M. Spuckler and R. Siegel, *J. Thermopysics Heat Transfer* **8**(1994) 193.